

Accurate estimation of the normalized mutual information of multidimensional data

Daniel Nagel,¹ Georg Diez,¹ and Gerhard Stock^{1, a)}

Biomolecular Dynamics, Institute of Physics, University of Freiburg, 79104 Freiburg, Germany.

(Dated: 18 July 2024)

While the linear Pearson correlation coefficient represents a well-established normalized measure to quantify the interrelation of two stochastic variables X and Y , it fails for multidimensional variables such as Cartesian coordinates. Avoiding any assumption about the underlying data, the mutual information $I(X, Y)$ does account for multidimensional correlations. However, unlike the normalized Pearson correlation, it has no upper bound ($I \in [0, \infty)$), i.e., it is not clear if say, $I = 0.4$ corresponds to a low or a high correlation. Moreover, the mutual information (MI) involves the estimation of high-dimensional probability densities (e.g., six-dimensional for Cartesian coordinates), which requires a k -nearest neighbor algorithm, such as the estimator by Kraskov et al. [Phys. Rev. E **69**, 066138 (2004)]. As existing methods to normalize the MI cannot be used in connection with this estimator, a new approach is presented, which uses an entropy estimation method that is invariant under variable transformations. The algorithm is numerically efficient and does not require more effort than the calculation of the (un-normalized) MI. After validating the method by applying it to various toy models, the normalized MI between the C_α -coordinates of T4 lysozyme is considered and compared to a correlation analysis of inter-residue contacts.

I. INTRODUCTION

Quantifying the correlation between different observables represents an essential aspect of data analysis across various disciplines. Examples include geostatistics, where the interrelationships of geographic variables in distinct spatial regions are studied,^{1–3} brain research that attempts to identify associations between various brain regions to gain insight into the functional pathways underlying cognitive processes,⁴ computer vision, which, e.g., aligns different images for tasks such as medical image analysis,^{5,6} and financial markets research that aims to gain insight into connections, market structures, and potential contagion effects during varying market conditions.^{7,8} In the field of chemical and biological physics, in particular, it is commonplace to study the dynamical correlation between atoms or various parts of a molecular system. For instance, correlation analysis is employed in principal component analysis that reduces the dimensionality of the system,^{9,10} in community detection approaches that identify interacting regions of a molecule,^{11–13} as well as in the construction of allosteric networks that aim to model signal transduction in proteins.^{14–17}

Most commonly, correlation is measured via the Pearson correlation coefficient ρ . It is defined as linear relationship between two (in general multidimensional) variables X and Y ,

$$\rho(X, Y) = \frac{\langle (X - \langle X \rangle)(Y - \langle Y \rangle) \rangle}{\sigma_X \sigma_Y}, \quad (1)$$

where $\langle \dots \rangle$ represents the statistical average and σ denotes the standard deviation. While the Pearson correlation coefficient is ubiquitous in statistical analysis,

it considers only the first two moments of the underlying distribution, which—strictly speaking—is adequate only for normally distributed data. Moreover, the linear definition turns out to be ill-defined to account for the correlation of multidimensional variables such as three-dimensional (3D) Cartesian coordinates.^{18,19}

The concept of mutual information (MI) goes beyond these limitations, because it avoids any assumption about the underlying data.²⁰ Taking into account two discrete random variables X and Y with their corresponding realizations $\mathcal{X} = \{x_i\}$ and $\mathcal{Y} = \{y_i\}$, the MI measures the statistical independence of X and Y by quantifying the dissimilarity of their joint probability distribution $p_{x,y}$ and the product of their marginal distributions $p_x p_y$ via the Kullback-Leibler divergence of these quantities.²¹ This leads to the definition

$$I(X, Y) = \sum_{x \in \mathcal{X}} \sum_{y \in \mathcal{Y}} p_{x,y} \ln \frac{p_{x,y}}{p_x p_y}, \quad (2)$$

which vanishes for independent variables satisfying $p_{x,y} = p_x p_y$. Introducing the Shannon entropy $H(X)$ and the joint entropy $H(X, Y)$ given by

$$H(X) = - \sum_{x \in \mathcal{X}} p_x \ln p_x, \quad (3)$$

$$H(X, Y) = - \sum_{x \in \mathcal{X}} \sum_{y \in \mathcal{Y}} p_{x,y} \ln p_{x,y}, \quad (4)$$

we may alternatively define the MI as

$$I(X, Y) = H(X) + H(Y) - H(X, Y), \quad (5)$$

$$= H(X) - H(X|Y). \quad (6)$$

Interpreting $H(X)$ as the uncertainty about X , and the conditional entropy $H(X|Y) = H(X, Y) - H(Y)$ as the uncertainty about X remaining after knowing Y , the MI

^{a)}Electronic mail: stock@physik.uni-freiburg.de

describes how much the uncertainty of X decreases when we gain insight into the variable Y . This intuitively appealing interpretation is readily generalized to the treatment of multivariate data, thus rendering MI a robust method to identify any associations between general variables.

Nevertheless, the practical application of the MI may face two (in part related) problems. Firstly, the computation of the MI from finite data can be challenging, because it relies on the accurate estimation of probability distributions p_x , p_y and $p_{x,y}$. Given 1D data, standard histogram or kernel-density estimation followed by numerical integration suffices to obtain accurate estimates of the MI.^{22,23} The estimation of multidimensional probability density functions, however, is notoriously difficult and plagued by the curse of dimensionality. For example, when we use Cartesian coordinates, the joint probability density function is six-dimensional. As a well-established solution, we may employ the algorithm by Kraskov, Stögbauer, and Grassberger,²⁴ also known as KSG-estimator, which uses Eq. (5) and estimates the entropies via a k -nearest neighbor (k -nn) algorithm.^{25–28}

Secondly, many applications require a normalization of the correlation measure. While this is naturally provided by the absolute Pearson correlation coefficient ($|\rho| \in [0, 1]$), the MI has no upper bound, $I(X, Y) \in [0, \infty)$. Given a specific value (say, $I(X, Y) = 0.4$), it is therefore *a priori* not clear whether this corresponds to a low or a high correlation. Recalling that the MI measures the decrease of the uncertainty of variable X when we get to know about variable Y [Eq. (6)], it is clear that the answer also depends on the uncertainties of the two individual variables, given by $H(X)$ and $H(Y)$. Hence, we need to normalize the MI to facilitate the comparison of the MI of different sets of variables or different systems.^{12,29,30} To this end, various strategies have been explored. For instance, a normalized MI (NMI) can be defined by assuming a normal joint distribution.^{19,31} Alternatively, a NMI can be achieved by discretizing the data onto a grid,³² although this might affect the statistical robustness of the resulting measure and can be significantly slower to compute compared to measures based on local k -nn statistics.³³

In this work, we present an alternative approach to normalize the MI, which exploits an entropy estimation method that is invariant under variable transformations and provides an upper bound for the MI. To this end, we first discuss the limitations of existing methods for estimating the NMI based on the k -nn approach and then describe the key concepts underlying our new method. Using the KSG-estimator,²⁴ the algorithm is highly scalable and may handle systems of high dimension. We validate our approach by applying it to various toy models, and compare to previous estimators. As a real-world example, we consider molecular dynamics simulation data of T4 lysozyme (T4L), a bistable protein consisting of 162 residues.^{34–36} To explain the functional motion of T4L, we calculate the NMI between the Cartesian coor-

dinates of all C_α -atoms, and compare the results to a MoSAIC¹³ correlation analysis of the inter-residue contacts of T4L. Our results demonstrate the effectiveness of our approach in accurately estimating the NMI of multi-dimensional variables.

II. THEORY AND METHODS

A. Normalizing the mutual information

To motivate a suitable normalization factor, we consider the well-known inequalities³⁷

$$\begin{aligned} I(X, Y) &\leq \min_{Z=X,Y} H(Z) \leq \sqrt{H(X)H(Y)} \\ &\leq \max_{Z=X,Y} H(Z) \leq H(X, Y). \end{aligned} \quad (7)$$

Aiming at a normalization that depends on both random variables, and since $I(X, X) = H(X)$, we choose the geometric mean because of its analogy to a normalized inner product and thus to the Pearson correlation coefficient.³⁰ This leads to the upper bound of the NMI defined as

$$I_N(X, Y) = \frac{I(X, Y)}{\sqrt{H(X)H(Y)}} \leq 1. \quad (8)$$

Unfortunately, however, the above inequalities hold only for discrete entropies but not for continuous entropies.³⁸ This poses a problem, as the KSG-estimator of the NMI is based on continuous k -nn statistics, which can violate Eq. (7). To facilitate the use of the inequalities, the discrete probability distributions (such as p_x) in the entropy definitions in Eqs. (3) and (4) must therefore be converted to continuous distributions (such as $P(x)$). With this end in mind, Shannon³⁹ suggested to use the continuous form

$$H_d(X) = - \int_{\mathcal{X}} dx P(x) \ln P(x), \quad (9)$$

referred to as 'differential' entropy. From the normalization condition

$$1 = \int_{\mathcal{X}} dx P(x), \quad (10)$$

it is obvious that the density $P(x)$ carries the dimension $1/[x]$, which causes a problem when calculating the entropy via $\ln P(x)$. Moreover, the normalization condition Eq. (10) may result in negative entropy estimates. To see this, we first consider the discrete case with normalization $1 \stackrel{!}{=} \sum_{x \in \mathcal{X}} p_x$, where every event occurs with a probability between zero and one (i.e., $p_x \leq 1$), which results in $\ln p_x \leq 0$ and ensures that the entropy is positive valued. In the continuous case, on the other hand, the probability density is normalized in Eq. (10) such that the area under its curve is one, which has the consequence that $P(x)$ can take any value in $[0, \infty)$. Thus, $\ln P(x) \in (-\infty, \infty)$, which results in an entropy that is not necessarily positive.

Jaynes³⁸ showed that the root cause of this problem lies in the lack of invariance of Eq. (9) under a variable transformation $x \rightarrow \tilde{x}$. He derived the correct continuous limit of the Shannon entropy,⁴⁰ referred to as 'relative' entropy

$$H_r(X) = - \int_{\mathcal{X}} dx P(x) \ln \frac{P(x)}{m(x)}, \quad (11)$$

where he introduced the invariant measure $m(x)$ that transforms identically to $P(x)$, i.e.,

$$x \rightarrow \tilde{x} : \quad \frac{P(x)}{m(x)} = \frac{P(\tilde{x})}{m(\tilde{x})}. \quad (12)$$

By design, the relative entropy $H_r(X)$ does not depend on the choice of coordinates or units.

Note that the invariant measure of two coordinates can be chosen to factorize in single-coordinate functions, i.e.,

$$m(x, y) = m(x)m(y), \quad (13)$$

because $m(x, y)$ must transform both variables like the respective coordinate. As a consequence, the MI remains invariant upon the introduction of the invariant measure,

$$\begin{aligned} I_d(X, Y) &= H_d(X) + H_d(Y) - H_d(X, Y) \\ &= H_r(X) + H_r(Y) - H_r(X, Y) + \int d(x, y) \\ &\quad \times P(x, y) \underbrace{[\ln m(x) + \ln m(y) - \ln m(x)m(y)]}_{=0} \\ &= I_r(X, Y), \end{aligned} \quad (14)$$

rendering the differential (subscript 'd') and relative (subscript 'r') definitions equivalent. It is important to stress, however, that this equivalence does not hold for the entropies, i.e., $H_d(X) \neq H_r(X)$, and therefore also not for the NMI in Eq. (8). Hence, it is crucial to apply relative entropies [Eq. (11)] when we compute the normalization between two continuous random variables. Otherwise, the usage of different representations or parametrizations of the two probability densities could lead to different results for the NMI, which renders it challenging to compare or interpret the results.

We note in passing that various alternative definition of the NMI exist. Obviously, we may simply divide the MI by its maximum I_{\max} , i.e.,

$$I_{\text{NM}}(X, Y) = \frac{I(X, Y)}{I_{\max}}. \quad (15)$$

Moreover, we can use the joint entropy from Eq. (7) and define

$$I_{\text{NJ}}(X, Y) = \frac{I(X, Y)}{H(X, Y)}. \quad (16)$$

Another approach is to employ the transformation of Gel'fand and Yaglom,^{19,31} i.e.,

$$I_{\text{GY}}(X, Y) = \sqrt{1 - \exp[-2I(X, Y)/(d_X + d_Y)]}, \quad (17)$$

where d_X and d_Y denote the dimension of variables X and Y , respectively. The definition of $I_{\text{GY}}(X, Y)$ clearly provides a mapping from the $I(X, Y) \in [0, \infty)$ to a normalized quantity. While this can be achieved by various mappings, I_{GY} can be shown to be identical to the linear correlation $|\rho|$ in the special case that $P(x, y)$ is a bivariate normal distribution. In the general case, however, the interpretation of I_{GY} as a correlation measure is less clear, because it does not take into account the upper bound of the mutual information based on the individual entropies of $H(X)$ and $H(Y)$, see Eq. (7). In particular, I_{GY} shows relatively large values already for weakly correlated data.¹³

B. KSG-estimator using the continuous entropy

While various continuous entropy estimators have been proposed,^{41–44} we wish to adapt the KSG-estimator²⁴ to compute the NMI, as it is able to treat multidimensional problems. The algorithm is based on local k -nn statistics, that is, it aims to calculate the probability distribution p_i of the distance between the data points $\{x_i\}$ and their k th nearest neighbor, assuming a local constant density. This probability can be visualized as the volume of a d -dimensional sphere with radius $2\varepsilon_i$, which is a proxy for the density of the points around x_i . The entropy is then given as the expectation value of $-\ln p_i$, which can be calculated from the digamma function ψ . For further reference, we only mention here the main results of the algorithm, and refer to the original paper for details.²⁴

Kraskov et al.²⁴ used the multinomial theorem to calculate the probability p_i and averaged the log-likelihood over all particles to obtain an estimate of the entropy. Starting with the definition of differential entropy in Eq. (9), they derived unbiased estimators \hat{H}_d for the differential entropy and the joint entropy

$$\begin{aligned} \hat{H}_d(X) &= -\langle \psi(n_x + 1) \rangle + \psi(N) + \ln c_{d_X} \\ &\quad + d_X \langle \ln 2\varepsilon \rangle, \end{aligned} \quad (18)$$

$$\begin{aligned} \hat{H}_d(X, Y) &= -\psi(k) + \psi(N) + \ln(c_{d_X} c_{d_Y}) \\ &\quad + (d_X + d_Y) \langle \ln 2\varepsilon \rangle. \end{aligned} \quad (19)$$

Here the first two terms of \hat{H}_d represent the average log-likelihood of finding the k th nearest neighbor distance ε , which can be expressed by the digamma function $\psi(n)$ that satisfies the recursion $\psi(n+1) = \psi(n) + 1/n$, with the Euler-Mascheroni constant as starting value $\psi(0) = -\gamma \approx 0.577$. Furthermore, N denotes the number of data points, $\langle \dots \rangle$ represents the average over these points, k is the number of nearest neighbors considered, ε is the distance between a considered data point and its k th nearest neighbor. Moreover, n_x is the number of points whose distance in x -direction from the considered data point is less than ε (analogously for n_y) and c_d is the volume of the d -dimensional unit ball.⁴⁵ Hence the latter two terms of \hat{H}_d account for the average log-volume of the k th nearest neighbor sphere. Inserting Eqs. (18) and

(19) into Eq. (5), we obtain the KSG-estimator of the MI

$$I(X, Y) = \psi(N) + \psi(k) - \langle \psi(n_x + 1) + \psi(n_y + 1) \rangle. \quad (20)$$

Using the differential entropy, the above estimator works perfectly fine to compute the (non-normalized) MI, since it is invariant with respect to a variable transformation due to Eq. (14). To calculate the normalized MI in Eq. (8), however, we need to ensure that the entropies $H(X)$ and $H(Y)$ are also invariant. Instead of the differential entropy, we therefore use the relative entropy estimator \hat{H}_r , which effectively introduces an additional term containing the invariant measure $m(X)$,

$$\hat{H}_r(X) = - \left\langle \ln \frac{p(X)}{m(X)} \right\rangle = \hat{H}_d(X) + \langle \ln m(X) \rangle \quad (21)$$

and analogously for $\hat{H}_r(X, Y)$. This results in the estimators

$$\begin{aligned} \hat{H}_r(X) = & - \langle \psi(n_x + 1) \rangle + \psi(N) + \ln c_{d_X} \\ & + d_X \langle \ln 2\varepsilon \rangle + \langle \ln m(X) \rangle, \end{aligned} \quad (22)$$

$$\begin{aligned} \hat{H}_r(X, Y) = & - \psi(k) + \psi(N) + \ln(c_{d_X} c_{d_Y}) \\ & + (d_X + d_Y) \langle \ln 2\varepsilon \rangle + \langle \ln m(X, Y) \rangle, \end{aligned} \quad (23)$$

which now additionally depend on the invariant measures $m(X)$ and $m(X, Y)$.

C. Estimating the Invariant Measures

Having ensured scale and parametrization invariance of the KSG-estimator via the introduction of invariant measures, the next step is to calculate these measures. To avoid bias, Jaynes³⁸ suggested using an invariant measure $m(X)$ that assumes complete ignorance, i.e., a constant probability density. For 1D data $\{x_i\}$ distributed between a and b , this yields

$$1 = \int_a^b m \, dx \Rightarrow m = \frac{1}{a - b}, \quad (24)$$

that is, the invariant measure is constant and defined via the boundaries of the data set. Although this ansatz makes sense for 1D problems, in higher dimensions it amounts to a uniform sampling of the data within a d -dimensional cube, which is hardly appropriate for finite data. In particular, data outliers may lead to a massive overestimation of the volume and thus to a significant underestimation of the density, resulting in an invalid estimate of the entropy.

To address this issue, we propose a new estimator of the invariant measure. Following Jaynes' suggestion,³⁸ we assume that the measures $m(X)$ and $m(X, Y)$ are the inverse of the corresponding volumes enclosed by the data points, i.e.,

$$m(X) = 1/V(X), \quad (25)$$

$$m(X, Y) = 1/V(X, Y). \quad (26)$$

To achieve an efficient estimation of the volumes, we only use quantities that are already computed in the original KSG-algorithm. As introduced in Eqs. (18)–(20), these include the distances ε between the data points and their k -th nearest neighbors, the number of points n whose distance from a considered data point is less than ε , and the volume c_d of the d -dimensional unit ball. To estimate the volume $V(X, Y)$, we calculate N times the mean volume of a single data point $\langle (2\varepsilon)^{d_X+d_Y} \rangle$, and divide it by the number of nearest neighbors k , to avoid overcounting. This yields the estimator

$$\hat{V}(X, Y) = \frac{N}{k} c_{d_X} c_{d_Y} \langle (2\varepsilon)^{d_X+d_Y} \rangle. \quad (27)$$

To ensure the factorization of the measure [Eq. (13)], we request that

$$\hat{V}(X, Y) = \hat{V}(X) \hat{V}(Y), \quad (28)$$

which leads directly to the invariant measures⁴⁶

$$\ln \hat{m}(X) = - \ln c_{d_X} - \frac{d_X}{d_X + d_Y} \ln \langle (2\varepsilon)^{d_X+d_Y} \rangle, \quad (29)$$

$$\ln \hat{m}(X, Y) = - \ln(c_{d_X} c_{d_Y}) - \ln \langle (2\varepsilon)^{d_X+d_Y} \rangle. \quad (30)$$

Inserting these expressions into Eqs. (22) and (23), we obtain as a final result the entropy estimators

$$\hat{H}_r(X) = - \langle \psi(n_x + 1) \rangle + \psi(N) + d_X \langle \ln \tilde{\varepsilon} \rangle, \quad (31)$$

$$\hat{H}_r(X, Y) = - \psi(k) + \psi(N) + (d_X + d_Y) \langle \ln \tilde{\varepsilon} \rangle, \quad (32)$$

where $\tilde{\varepsilon} = \varepsilon / \langle \varepsilon^{d_X+d_Y} \rangle^{1/(d_X+d_Y)}$ denotes the scaling-invariant k -nn radius. Equations (29)–(32) represent the main theoretical results of this paper. As the inequalities in Eq. (7) apply for the above entropy estimators \hat{H}_r , the NMI can be obtained through the normalization factor $(\hat{H}_r(X) \hat{H}_r(Y))^{-\frac{1}{2}}$ as in Eq. (8), or alternatively via the factor $\hat{H}_r(X, Y)^{-1}$ as in Eq. (16). We note that Eqs. (29)–(32) address the two main challenges in computing MI: accurately estimating probability distributions in high-dimensional spaces with finite data, and normalizing MI for meaningful comparisons across different data sets. The first challenge is addressed by using k -nearest neighbor statistics to approximate probability distributions; the second one by normalizing MI using relative entropy, which is achieved by introducing an invariant measure that assumes a constant density.

Apart from the mean volume-based approach discussed above, we also derived and discussed a mean radius-based algorithm for the volume estimator. It is defined as N times the volume of a d -dimensional sphere c_d (with the average radius of the k th nearest neighbor) divided by k , see the SI. While both algorithms are quite similar, the radius-based estimator suffers from a systematic bias for small values of k caused by boundary effects, leading to an underestimation of the volume, see Fig. S1 in the Supplementary Material.

D. Validation

Let us first test the accuracy of the volume estimator in Eq. (27) for simple example distributions. To this end, Fig. 1 shows estimations of $V(X)$ as a function of the sample size N , obtained for various numbers of nearest neighbors k . For easy representation, we divide $\hat{V}(X)$ by the exact volume $V_{\text{ex}}(X)$, such that the ratio approaches 1 for large N . Moreover, we average over 100 calculations of \hat{V} , in order to suppress large fluctuations of $\hat{V}(X)$ for small N . In the case of a 2D uniform distribution ($x, y \in [0, 1]$), we find that the k -nn estimator converges rapidly to the correct result, and depends (for not too small N) only little on k (Fig. 1a). We also estimate the volume from the boundaries of the data set according to Eq. (24), i.e., $\hat{V}_{\text{max}} = (x_{\text{max}} - x_{\text{min}})(y_{\text{max}} - y_{\text{min}})$. As expected, the latter ansatz works perfectly well for a uniform distribution. The situation is different in our second example, where the data are uniformly distributed in a donut-shaped area (Fig. 1b). While the boundary-based estimation again gives the full 2D area (which in the present example is too large by $\sim 70\%$), the k -nn estimator reliably converges to the correct result.

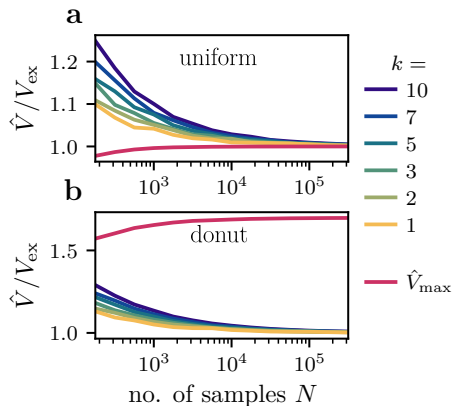


FIG. 1. Estimation of the volume of (a) a uniform distribution ($x, y \in [0, 1]$) and (b) uniformly distributed data on a donut-shaped area with $r = \sqrt{x^2 + y^2} \in [0.5, 1]$. Shown as a function of the sample size N , results of the k -nn estimator [Eq. (27)] for various numbers k of nearest neighbors are compared to the boundary estimate \hat{V}_{max} [Eq. (24)].

Next we wish to assess the accuracy and performance of the new estimator of the NMI defined in Eq. (8). To this end, we employ a 2D toy model with the distribution

$$P(r = \sqrt{x^2 + y^2}) \propto \exp \left[-\frac{(r - r_0)^2}{2\sigma^2} \right], \quad (33)$$

with mean $r_0 = 0.75$ and standard deviation $\sigma = 1/8$. In the following, we compare the results of our k -nn estimator I_N with $k = 5$ to other commonly used methods.

We first compare the results for I_N to the most commonly used method, that is, the binning of the variables. This discrete estimation of the NMI $I_{N,\text{hist}}$ appears rather simple and is expected to yield good results for 2D data.¹²

It should be stressed, though, that for finite data, the entropy estimates (and thus the NMI) depend considerably on the number of bins N_{bins} used per dimension. Comparing the NMI obtained for various choices of N_{bins} and sample sizes N , Fig. 2a shows that the accuracy of the binning approach indeed depends critically on these parameters. While most of the choices clearly overestimate the NMI, we find that the previously suggested heuristic of selecting the number of bins to minimize the NMI achieves the closest approximation to our k -nn estimator result.¹²

Generally speaking, the assumption of a uniform probability distribution $P(x) = N_{\text{bins}}^{-1}$ leads to $H(X) = \ln N_{\text{bins}}$, which diverges as N_{bins} approaches infinity. For finite sampling and bin numbers, on the other hand, the entropy is maximized once there is only a single point in each bin. This limit leads to $P(x) = 1/N = P(x, y)$ and thus to an NMI of 1. Defining H_{max} as the largest possible entropy for a given number of samples N , we thus find that both estimators, N_N and $N_{N,\text{hist}}$, exhibit a $1/H_{\text{max}}$ scaling with N . When we multiply the results for the k -nn estimator I_N and for the binning method $I_{N,\text{hist}}$ with H_{max} , Fig. 2b indeed reveals that the resulting quantities depend only minor on N . Due to the simplicity of the model, the fluctuations of the NMIs (shaded areas) become smaller than the line width for $N \gtrsim 10^3$.

To demonstrate the necessity of introducing an invariant measure to calculate I_N , Fig. 2b also shows results for $I_{N,d}$, which were obtained by directly using the differential entropy [Eq. (9)] for the NMI estimator.⁴⁷ Getting negative values for the NMI in our model example, this is clearly not an option. Fig. 2b also shows the NMI of Gel'fand and Yaglom [Eq. (17)], which is significantly larger than the values obtained from the k -nn estimator and for the binning method.

Finally, we briefly discuss the effort to compute the proposed estimators. The estimator scales with the number of samples N as $\mathcal{O}(N \ln N)$, due to the k -d tree used for the nearest neighbor search. With respect to the number of coordinates M , we get the obvious scaling of $\mathcal{O}(M^2)$. We wish to stress that the NMI comes at the same price as the MI, since the ingredients of the normalization factor (e.g., $H(X)$) are calculated anyway. Let us mention some runtimes examples for the new NMI estimator, using an Intel® Core™ i9-10900 CPU. For $N = 10^5$ samples and 230 1D coordinates, the computation of the 230×230 NMI matrix takes about 1 CPU hour. A similar time is needed to calculate the NMI matrix for $N = 10^4$ samples and 190 3D coordinates. For further details, see Fig. S2.

III. APPLICATION: FUNCTIONAL DYNAMICS OF T4L

A. Model system

As an interesting and non-trivial example, we apply the new algorithm to explain the interresidue correlations associated with the functional dynamics of T4 lysozyme (T4L).^{34–36} Aiming to destroy bacterial cell walls by cat-

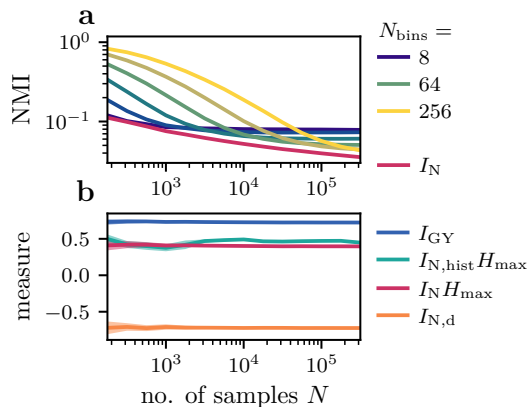


FIG. 2. Estimation of the NMI for the 2D model defined in Eq. (33), shown as a function of the sample size N . (a) Comparison of I_N obtained from the k -nn estimator to the discrete estimation of the NMI $I_{N,\text{hist}}$ obtained via 2D binning of the data using various numbers of bins $N_{\text{bins}} \in [8, 256]$. (b) Comparison of various estimations for the NMI, indicating the respective standard deviation by a shaded area. Shown are the k -nn estimator $I_N H_{\text{max}}$ ($k = 5$), the 2D binning result $I_{N,\text{hist}} H_{\text{max}}$ ($N_{\text{bin}} \in [8, 256]$), the NMI I_{GY} of Gel’fand and Yaglom [Eq. (17)], and $I_{N,d}$ using the differential entropy [Eq. (20)]. Here H_{max} corresponds to the highest possible entropy (i.e., the entropy of a uniform distribution for a given number of samples N). For each value of N , we average over 100 calculations.

alyzing the cleavage of glycosidic bonds, T4L performs an open-closed transition of its two domains that resembles a Pac-Man, see Figs. 3a,b. This motion of the “mouth” region was recently shown to be triggered by a locking mechanism in the “hinge” region of T4L, by which the side chain of Phe4 changes from a solvent-exposed to a hydrophobically-buried state.³⁵ To elucidate the mechanism underlying this long-range (or allosteric) coupling between the two distant regions, various dimensionality reduction approaches have been employed.^{35,48–51} Applying the MoSAIC¹³ correlation analysis to all interresidue contacts of T4L, a network of interresidue distances was identified (Fig. 4a), which move in a concerted manner.⁵² The cooperative process originates from a cogwheel-like motion of the hydrophobic core in the hinge region, which constitutes a flexible transmission network. Through rigid contacts and the protein backbone, the small local changes of the hydrophobic core are passed on to the distant terminal domains and lead to the emergence of a rare global conformational transition.

Given this exceptionally well-studied example of allosteric coupling, it is instructive to further characterize the underlying conformational transition by considering the NMI of the C_α -atom coordinates. The resulting correlation matrix constitutes a residue interaction network, which is commonly employed to reveal allosteric pathways using network theory methods.^{14–17} To this end, we adopt the 50 μs -long all-atom molecular dynamics (MD) simulation by Ernst et al.³⁵, which employed Gromacs

4.6.7⁵³ in combination with the Amber ff99SB*-ILDN force field^{54–56} and the TIP3P water model.⁵⁷

Using Cartesian C_α -atom coordinates, first the translation and overall rotation must be removed from the MD trajectory. Since the rotation depends via the moment of inertia on the molecule’s structure, this separation is only straightforward for rigid systems, but can lead to serious artifacts when we calculate the linear correlation matrix [Eq. (1)] of molecules that undergo large-amplitude motion (as, e.g., folding proteins).⁵⁸ Although being scale-invariant with respect to linear coordinate transformations,²⁰ this problem also occurs for the MI. To test if this is an issue when considering the open-closed motion of T4L, we performed a global rotational fit (where both open and closed conformations are rotated with respect to a common reference structure) and a local rotational fit (where the open and closed conformations are rotated with respect to their respective reference structure). Comparing the resulting estimates of the linear correlation and the NMI, Fig. S3 reveals only minor differences, suggesting that the standard rotational fit procedure works satisfactorily to describe the functional dynamics T4L.

B. Comparison of correlation measures

The 50 μs -long MD trajectory of T4L populates the open and the closed state for $\sim 70\%$ and 30% of the time, respectively, and exhibits mean waiting times of $\tau_{o \rightarrow c} \sim 4 \mu\text{s}$ and $\tau_{c \rightarrow o} \sim 2 \mu\text{s}$, which are in excellent agreement with recent experimental results.⁵⁹ Applying the new algorithm to the MD data, Fig. 3c shows the resulting NMI matrix I_N obtained for the C_α -atom coordinates. As may be expected, we find large values of I_N along the diagonal, revealing strong correlations with the first next-neighbor residues. In well-defined secondary structures such as the α -helices this extends typically to 3–4 next neighbors, in the connecting loops only to 1–2. Moreover, the matrix roughly splits up in four blocks, which are defined by the N-domain (α_1 – α_3 , β_1 – β_3) and the C-domain (α_5 – α_9), see Fig. 3a. While the diagonal blocks account for the internally quite rigid two domains, the less prominent off-diagonal blocks indicate correlated motions of the N- and C-domain. The α_4 -helix between the two domains couples only weakly to the adjacent helices and therefore acts as a lowly correlated buffer zone. This is because it lacks polar contacts with neighboring helices. At the C-terminal end, the α_{10} -helix is considerably exposed to the solvent and therefore correlates less with the core of the protein.

It is interesting to compare the above results for the NMI to the linear Pearson correlation coefficient defined in Eq. (1). Choosing the variables $X = (x_i, y_i, z_i)^T$ and $Y = (x_j, y_j, z_j)^T$ for the C_α -coordinates of residues i and j , respectively, the absolute Pearson coefficient is given as the sum of three directional components with $\alpha = x, y, z$

$$|\rho_{ij}| = \left| \sum_{\alpha} \rho_{ij}^{\alpha\alpha} \right|. \quad (34)$$

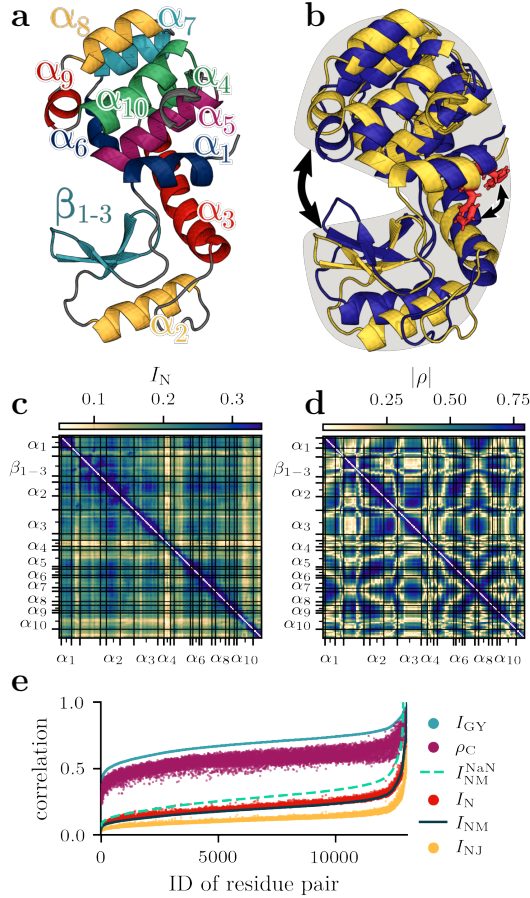


FIG. 3. Correlation analysis of the functional dynamics of T4 Lysozyme, using the Cartesian coordinates of all C_α atoms. Molecular structure of T4L, with panel (a) indicating the secondary structures, and panel (b) showing the open (yellow) and closed (blue) conformations. The open-closed motion of the mouth region by a black arrow and the locking mechanism in the hinge region by residue Phe4 (red). (c) k -nn estimation [Eq. (8)] of the NMI and (d) corresponding absolute Pearson correlation coefficient [Eq. (1)]. (e) Comparison of various correlation measures, displayed in the order of increasing values of the (un-normalized) MI of all residue pairs. Shown are our standard definition $I_N = I/\sqrt{H(X)H(Y)}$, the variant using the joint entropy $I_{NJ}(X, Y) = I(X, Y)/H(X, Y)$, the maximum-normalized $I_{NM}(X, Y) = I(X, Y)/I_{\max}$, the maximum-normalized I_{\max}^{NaN} that neglects next-neighbor correlations, $I_{GY} = \sqrt{1 - \exp(-I/3)}$ according to Gel'fand and Yaglom, and the canonical correlation ρ_C .

That is, due to the scalar product in Eq. (1), only diagonal elements of $\rho_{ij}^{\alpha\beta}$ with $\alpha = \beta$ occur. Comparing the results for the Pearson coefficient and the NMI, Figs. 3c and 3d show that the two correlation measures differ substantially, i.e., the structure of the Pearson matrix shows prominent patterns that are absent in the NMI. This artifact of the Pearson coefficient is due to the fact that the components $\rho_{ij}^{\alpha\alpha}$ at the same time account for the correla-

tion between residues i and j and the relative orientation of the directions $\alpha = x, y, z$. Since the components can take positive and negative values ($-1 \leq \rho_{ij}^{\alpha\alpha} \leq 1$), for example, a large positive value for ρ_{ij}^{xx} can be canceled by a large negative value for ρ_{ij}^{yy} , although residues i and j are highly correlated. Showing the matrices of the three components ρ_{ij}^{xx} , ρ_{ij}^{yy} , and ρ_{ij}^{zz} , Fig. S4 readily explains the spurious pattern of the Pearson correlation matrix. Although this failure of the Pearson measure for Cartesian coordinates was previously pointed out by Lange and Grubmüller,¹⁹ the Pearson correlation coefficient nevertheless has seen widespread use in the construction of allosteric networks.^{14–17}

As a simple remedy, we may sum the moduli of the three components, i.e., $|\rho_{ij}| = \sum_\alpha |\rho_{ij}^{\alpha\alpha}|$, which results in an improved linear correlation matrix, that is more similar to the NMI, see Fig. S5a. More rigorously, we employ canonical correlation analysis (CCA) as a standard tool of multivariate statistical analysis,⁶⁰ which was previously used to calculate the linear correlation between Cartesian coordinates.⁶¹ Introducing linear transformations $A, B \in \mathbb{R}^{3 \times 3}$ of the original coordinates X and Y , CCA calculates the canonical variables $\hat{X} = AX$ and $\hat{Y} = BY$, which maximize the canonical correlation

$$\rho_C(X, Y) \equiv \rho(\hat{X}, \hat{Y}) \stackrel{!}{=} \max. \quad (35)$$

This leads to an eigenvalue problem for the canonical variables \hat{X} and \hat{Y} , which yields the canonical correlation from a sum of the eigenvalues, i.e., $\rho_C^2 = \frac{1}{3} \sum_i \lambda_i$. As shown in the SI, the eigenvalues can be calculated directly from the 3×3 correlation matrices, which renders CCA a rather efficient method. Comparing the resulting CCA matrix to the NMI, Fig. S5b reveals good overall agreement of the two correlation measures. As first discussed by Lange and Grubmüller,¹⁹ this shows that the main discrepancy between the Pearson correlation and the NMI is due to the lack of an appropriate treatment of the relative orientation of the components, rather than intrinsically nonlinear correlation effects.

As contour plots of similar correlation matrices look very much the same, we change to an alternative representation to compare various versions of the NMI. That is, we sort the $\sim 13\,000$ residue pairs in the order of increasing values of the (un-normalized) mutual information I , such that I is a monotonically increasing function. Using this ordering, Fig. 3e compares the following variants of the NMI:

- $I_{NM}(X, Y) = I(X, Y)/I_{\max}$,
- $I_N(X, Y) = I(X, Y)/\sqrt{H(X)H(Y)}$,
- $I_{NJ}(X, Y) = I(X, Y)/H(X, Y)$,
- $I_{GY}(X, Y) = \sqrt{1 - \exp(-I(X, Y)/3)}$,
- and $\rho_C(X, Y)$ defined in Eq. (35).

The first three measures look quite similar, that is, they start at ~ 0.06 , exhibit a slow, approximately linear increase until $\sim 12\,000$, before they show a rapid rise to its final value of 1. That is, the vast majority (more than $\sim 90\%$) of residue pairs show a correlation of I/I_{\max} between 0.1 and 0.3. This is in clear difference to I_{GY} that is significantly shifted to higher values such that the majority ($\sim 90\%$) of residue pairs show a correlation between 0.5 and 0.8. This means, for example, that two weakly correlated residues with $I_N = 0.2$ yield $I_{GY} \approx 0.7$, which seems to indicate considerable correlation. Hence, the interpretation of I_{GY} might be misleading, although the limit for normally distributed variables is given by the Pearson coefficient and therefore well defined. The canonical correlation ρ_C , shows also rather high values and significant vertical spread of the data. Presumably, the latter finding is caused by nonlinear effects that are not described by the linear measure ρ_C .

We now focus on the first three measures. First we note that our standard definition I_N follows the maximum-normalized I_{NM} very closely and shows a rather small average spread of approximately 0.04. $I/H(X, Y)$ behaves quite similar, but is shifted to smaller values due to Eq. (7). The overall agreement of these two measures with I/I_{\max} reveals that the respective normalization factors $1/\sqrt{H(X)H(Y)}$ and $1/H(X, Y)$ are roughly constant and depend only little on the considered residue pair. As shown in Eqs. (31) and (32), this dependence enters solely via the function ϵ , representing the distance between a considered data point and its k th neighbor. For a densely packed protein such as T4L, ϵ appears to be quite similar for all residue pairs, and causes only a small vertical spread of I_N and $I/H(X, Y)$.

The excellent agreement of I_N with I/I_{\max} seems to validate I_N as standard definition of the NMI. We note, however, that the applicability of the maximum-normalized I/I_{\max} requires the existence of at least one perfectly correlated data point (i.e., with $I_N \approx 1$). In the case of proteins, this is typically obtained for directly neighboring residues. In contrast, when we use a data set with $I_N \ll 1$ this agreement breaks down. For example, by excluding next-neighbor correlations of T4L, the resulting maximum-normalized quantity I_{\max}^{NaN} shifts towards larger values (Fig. 3e), and does no longer agree with I_N .

C. Interresidue NMI vs contact correlation

We finally discuss the ability of the C_α -based NMI to explain the mechanism of the open-close transition in T4L. Let us first recap previous results,³⁶ which were based on the analysis of interresidue contacts. As explained above, the open-close transition of the mouth region (including the β -sheets of the N-domain and the helices α_5 and α_9 of the C-domain) is triggered by the locking motion of Phe4 in the hinge region (including the helices α_1 and α_3). The cooperative process is mediated via a network of ~ 30 highly correlated contacts,⁵² which

range from the hinge region to the mouth, see Fig. 4a. Indicated by red dots, Fig. 4c shows that these contacts in particular connect helices α_1 and α_3 in the hinge region, as well as β -sheets β_1 – β_3 and helices α_5 and α_9 in the mouth region. For example, during the open-closed transition, in the hinge region the salt bridge between Glu5 and Lys60 opens, while in the mouth region the salt bridges Asp20-Arg145 and Glu22-Arg137 close.

We note that correlated contacts identified by MoSAIC¹³ typically show a high difference of their population probabilities $\Delta p = p_{\text{open}} - p_{\text{closed}}$ to exist in the open and the closed state, see Tab. S1. That is, 20 contacts exhibit $\Delta p \gtrsim 0.7$, meaning that the contact approximately is open in one state and closed in the other state. The remaining 12 MoSAIC contacts showed $\Delta p \lesssim 0.2$, corresponding to a small (but correlated) change of the contact distance. We also found ~ 10 contacts with moderate population changes (between 0.3 and 0.7) and correlations (between 0.2 and 0.5). While a large population change clearly indicate the participation of a contact in an allosteric transition,^{62,63} highly correlated contacts as identified by Mosaic moreover indicate a cooperative process.

To relate the above contact-based switching mechanism to the information that can be learned from the C_α -based NMI of T4L, it is helpful to describe the open and the closed state separately and consider the difference of the NMI in both conformations

$$\Delta I = I_N^{\text{closed}} - I_N^{\text{open}}, \quad (36)$$

the modulus of which is shown in Fig. 4c. Interestingly, ΔI is found to overall decrease in the closed state (i.e., $\Delta I < 0$), except for the α_4 -helix separating the two domains of T4L. As two rigidly connected residues are highly correlated, while flexibly connected residues are less so, we can typically associate high correlation with a relatively rigid connection (since a rigid connection allows for an easy prediction of the position of one part by knowing the position of the other). That is, $\Delta I_{ij} < 0$ means that the residues i and j are more rigidly coupled in the open state. This is in line with the root-mean-square-fluctuations of T4L (Fig. S6), which are overall enhanced in the open state, except for helices α_4 and α_{10} whose fluctuations are similar. To facilitate the interpretation of the NMI difference matrix ΔI_{ij} , Fig. 4b reveals a network representation of the most important interactions (shown as blue patches in Fig. 4c). Restricting ourselves to $|\Delta I_{ij}| \geq 0.06$, we find that (almost) all high NMI differences involve the α_1 -helix. In this sense, the blue lines that connect α_1 to the N-domain and the C-domain can be considered as allosteric pathways.

When we compare the coupling networks in Figs. 4a and 4b, we see that both the contact-based representation and the NMI difference matrix highlight the α_1 -helix (including key residue Phe4) as the main driver of the open-closed process. While the contact changes identified by MoSAIC account for the origin of the conformation transition (i.e., the cooperative breaking and mak-

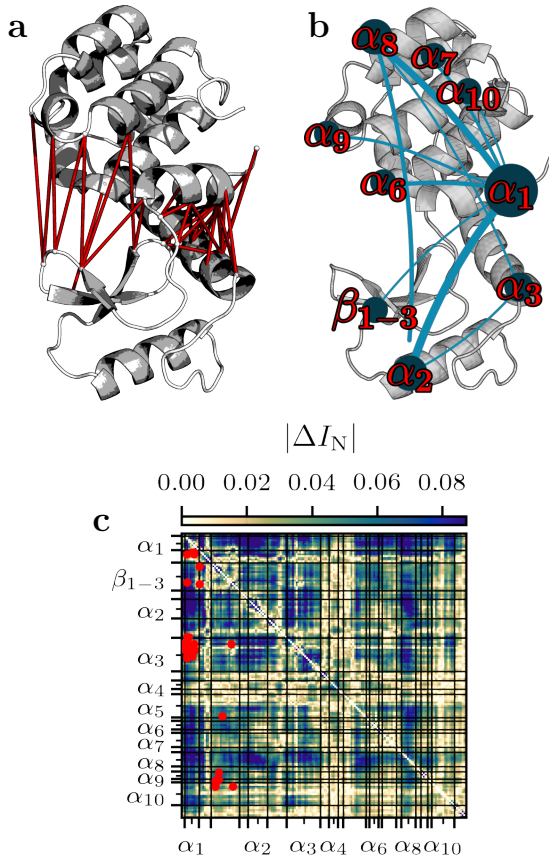


FIG. 4. Illustration of the main structural correlations of T4L during the open-closed transition. (a) Network of correlated inter-residue contacts identified by MoSAIC.¹³ (b) Network representation of the most significant changes of the NMI, $\Delta I = I_N^{\text{closed}} - I_N^{\text{open}}$. The edge width reflects the average $|\Delta I|$ between two secondary structures, showing only edges with $|\Delta I| \geq 0.06$. (c) Matrix representation of $|\Delta I|$, which also shows the MoSAIC contacts (red dots).

ing of contacts during the transition), the C_α -based NMI differences rather report on the change in rigidity of the system, that is, on the impact of the transition.

IV. CONCLUDING REMARKS

We have generalized the widely used KSG-estimator²⁴ of the mutual information (MI) to facilitate the calculation of the normalized MI (NMI). The normalization is achieved by introducing the relative entropy, which is invariant under variable transformations.³⁸ Our new estimator of the NMI correctly reproduces results of a histogram-based calculation for one-dimensional problems, but is beyond that capable of treating multi-dimensional systems due to the use of k -nn statistics. The algorithm is numerically efficient and does not require more effort than the calculation of the (un-normalized) MI.

Considering the open-closed transition of T4L as a well-studied example of allosteric coupling, we have calculated the NMI of the C_α -atom coordinates. Comparing various correlation measures, we demonstrated that the k -nn-based estimation I_N represents a correct upper bound of the NMI (assuming normalization factors that contain both variables) and agrees well with the maximum-normalized MI I/I_{max} (if the data contain at least one perfectly correlated point). Conversely, we showed that the popular rescaled measure $I_{\text{GY}} = \sqrt{1 - \exp(-I/3)}$ typically overestimates the correlation significantly. We also showed that the linear Pearson correlation coefficient ρ_{ij} fails completely to reproduce the correct NMI of Cartesian coordinates, while the linear canonical correlation analysis^{60,61} was found to yield qualitatively correct results at low computational cost. Finally we discussed the merits of the C_α -based NMI to explain the structural mechanism of the open-closed transition of T4L.

Supplementary material

Supplementary methods include the description of the radius-based algorithm for the volume estimator (Fig. S1), the runtime comparison (Fig. S2) and the canonical correlation analysis (Fig. S5). Supplementary results for T4L include rotational fit analysis (Fig. S3), spatial components of the Pearson correlation (Fig. S4), the RMSF (Fig. S6), and Tab. S1 listing important interresidue contacts.

Acknowledgments

The authors thank Steffen Wolf and Nele Dethloff for helpful comments and discussions. This work has been supported by the Deutsche Forschungsgemeinschaft (DFG) within the framework of the Research Unit FOR 5099 "Reducing complexity of nonequilibrium" (project No. 431945604), the High Performance and Cloud Computing Group at the Zentrum für Datenverarbeitung of the University of Tübingen, the state of Baden-Württemberg through bwHPC and the DFG through grant no INST 37/935-1 FUGG (RV bw16I016), and the Black Forest Grid Initiative.

Data Availability Statement

The estimator is freely available at <https://github.com/moldyn/normi>, or via `pip/conda install normi`, and adapts the scikit-learn syntax.⁶⁴

¹A. D. Cliff and J. K. Ord, *Spatial processes: models & applications*, Pion, 1981.

²D. Wartenberg, Multivariate spatial correlation: a method for exploratory geographical analysis, *Geogr. Anal.* **17**, 263 (1985).

³P. Legendre, Spatial autocorrelation: trouble or new paradigm?, *Ecology* **74**, 1659 (1993).

⁴B. B. Averbeck, P. E. Latham, and A. Pouget, Neural correlations, population coding and computation, *Nat. Rev. Neurosci.* **7**, 358 (2006).

⁵P. Viola and W. M. Wells III, Alignment by maximization of mutual information, *Int. J. Comput. Vis.* **24**, 137 (1997).

- ⁶J. P. Pluim, J. A. Maintz, and M. A. Viergever, Mutual information-based registration of medical images: a survey, *IEEE Trans. Med. Imaging* **22**, 986 (2003).
- ⁷O. E. Barndorff-Nielsen and N. Shephard, Econometric analysis of realized covariation: High frequency based covariance, regression, and correlation in financial economics, *Econometrica* **72**, 885 (2004).
- ⁸X. Guo, H. Zhang, and T. Tian, Development of stock correlation networks using mutual information and financial big data, *PLoS one* **13**, e0195941 (2018).
- ⁹A. Amadei, A. B. M. Linssen, and H. J. C. Berendsen, Essential dynamics of proteins, *Proteins* **17**, 412 (1993).
- ¹⁰I. T. Jolliffe, *Principal Component Analysis*, Springer, New York, 2002.
- ¹¹C. L. McClendon, A. P. Kornev, M. K. Gilson, and S. S. Taylor, Dynamic architecture of a protein kinase, *Proc. Natl. Acad. Sci. USA* **111**, E4623 (2014).
- ¹²P. Ravindra, Z. Smith, and P. Tiwary, Automatic mutual information noise omission (AMINO): generating order parameters for molecular systems, *Mol. Syst. Des. Eng.* **5**, 339 (2020).
- ¹³G. Diez, D. Nagel, and G. Stock, Correlation-based feature selection to identify functional dynamics in proteins, *J. Chem. Theory Comput.* **18**, 5079 – 5088 (2022).
- ¹⁴A. Sethi, J. Eargle, A. A. Black, and Z. Luthey-Schulten, Dynamical networks in tRNA:protein complexes, *Proc. Natl. Acad. Sci. USA* **106**, 6620 (2009).
- ¹⁵C. L. McClendon, G. Friedland, D. L. Mobley, H. Amirkhani, and M. P. Jacobson, Quantifying correlations between allosteric sites in thermodynamic ensembles, *J. Chem. Theory Comput.* **5**, 2486 (2009).
- ¹⁶M. Bhattacharyya, S. Ghosh, and S. Vishveshwara, Protein structure and function: Looking through the network of side-chain interactions, *Curr. Prot. Pept. Sci.* **17**, 4 (2016).
- ¹⁷S. J. Wodak et al., Allostery in its many disguises: From theory to applications, *Structure* **27**, 566 (2019).
- ¹⁸T. Ichiye and M. Karplus, Collective motions in proteins: A covariance analysis of atomic fluctuations in molecular dynamics and normal mode simulations, *Proteins* **11**, 205 (1991).
- ¹⁹O. F. Lange and H. Grubmüller, Generalized correlation for biomolecular dynamics, *Proteins* **62**, 1053 (2006).
- ²⁰T. M. Cover and J. A. Thomas, *Elements of Information Theory*, Wiley, 2006.
- ²¹C. L. McClendon, L. Hua, G. Barreiro, and M. P. Jacobson, Comparing conformational ensembles using the Kullback–Leibler divergence expansion, *J. Chem. Theory Comput.* **8**, 2115 (2012).
- ²²B. W. Silverman, *Density Estimation for Statistics and Data Analysis*, Chapman and Hall, 1986.
- ²³D. W. Scott, *Multivariate density estimation: theory, practice, and visualization*, John Wiley & Sons, 2015.
- ²⁴A. Kraskov, H. Stögbauer, and P. Grassberger, Estimating mutual information, *Phys. Rev. E* **69**, 066138 (2004).
- ²⁵L. F. Kozachenko and N. N. Leonenko, Sample estimate of the entropy of a random vector, *Probl. Peredachi. Inf.* **23**, 9 (1987).
- ²⁶A. B. Tsybakov and E. C. van der Meulen, Root-n consistent estimators of entropy for densities with unbounded support, *Scand. J. Stat.* **23**, 75 (1996).
- ²⁷H. Singh, N. Misra, V. Hnizdo, A. Fedorowicz, and E. Demchuk, Nearest neighbor estimates of entropy, *Am. J. Math.* **23**, 301 (2003).
- ²⁸D. Lombardi and S. Pant, Nonparametric k -nearest-neighbor entropy estimator, *Phys. Rev. E* **93**, 013310 (2016).
- ²⁹C. Studholme, D. Hill, and D. Hawkes, An overlap invariant entropy measure of 3d medical image alignment, *Pattern Recognit.* **32**, 71 (1999).
- ³⁰A. Strehl and J. Ghosh, Cluster ensembles—a knowledge reuse framework for combining multiple partitions, *J. Mach. Learn. Res.* **3**, 583 (2002).
- ³¹I. M. Gel’fand and A. M. Yaglom, Computation of the amount of information about a stochastic function contained in another such function, *Transl.- Am. Math. Soc.* **12** (1959).
- ³²D. N. Reshef, Y. A. Reshef, H. K. Finucane, S. R. Grossman, G. McVean, P. J. Turnbaugh, E. S. Lander, M. Mitzenmacher, and P. C. Sabeti, Detecting novel associations in large data sets, *Science* **334**, 1518 (2011).
- ³³J. B. Kinney and G. S. Atwal, Equitability, mutual information, and the maximal information coefficient, *Proc. Natl. Acad. Sci. U.S.A.* **111**, 3354 (2014).
- ³⁴M. Dixon, H. Nicholson, L. Shewchuk, W. Baase, and B. Matthews, Structure of a hinge-bending bacteriophage T4 lysozyme mutant, Ile3→Pro, *J. Mol. Biol.* **227**, 917 (1992).
- ³⁵M. Ernst, S. Wolf, and G. Stock, Identification and validation of reaction coordinates describing protein functional motion: Hierarchical dynamics of T4 Lysozyme, *J. Chem. Theory Comput.* **13**, 5076 (2017).
- ³⁶M. Post, B. Lickert, G. Diez, S. Wolf, and G. Stock, Cooperative protein allosteric transition mediated by a fluctuating transmission network, *J. Mol. Bio.* **434**, 167679 (2022).
- ³⁷N. X. Vinh, J. Epps, and J. Bailey, Information theoretic measures for clusterings comparison: Variants, properties, normalization and correction for chance, *J. Mach. Learn. Res.* **11**, 2837 (2010).
- ³⁸E. T. Jaynes, Prior probabilities, *IEEE T. Syst. Sci. Cyb.* **4**, 227 (1968).
- ³⁹C. E. Shannon, A mathematical theory of communication, *Bell Syst. Tech. J.* **27**, 379 (1948).
- ⁴⁰In taking the limit $N \rightarrow \infty$, Jaynes encountered an additional diverging term $\ln N$, which is usually omitted³⁸.
- ⁴¹I. Nemenman, F. Shafee, and W. Bialek, Entropy and inference, revisited, in *Advances in Neural Information Processing Systems*, edited by T. Dietterich, S. Becker, and Z. Ghahramani, volume 14, MIT Press, 2001.
- ⁴²J. Jiao, K. Venkat, Y. Han, and T. Weissman, Minimax estimation of functionals of discrete distributions, *IEEE Trans. Inf. Theory* **61**, 2835 (2015).
- ⁴³E. Archer, I. M. Park, and J. W. Pillow, Bayesian entropy estimation for countable discrete distributions, *J. Mach. Learn. Res.* **15**, 2833 (2014).
- ⁴⁴G. Valiant and P. Valiant, Estimating the unseen: Improved estimators for entropy and other properties, *Journal of the ACM* **64**, 1 (2017).
- ⁴⁵To minimize bias due to different radii in the joint and marginal spaces, they estimate marginal entropies not with a fixed k but with a fixed ϵ taken from the joint entropy. So if the ϵ_i ball at x_i contains n_{x_i} points, the distance corresponds to the $n_{x_i} + 1$ nearest-neighbor distance.
- ⁴⁶As in Jaynes’ derivation of the relative entropy,³⁸ we neglect the term $\ln N$.
- ⁴⁷C. X. Hernández and V. S. Pande, Mdentropy: Information-theoretic analyses for molecular dynamics, *J. Open Source Soft.* **2**, 427 (2017).
- ⁴⁸J. S. Hub and B. L. de Groot, Detection of functional modes in protein dynamics, *PLoS Comput. Biol.* **5**, e1000480 (2009).
- ⁴⁹O. F. Lange and H. Grubmüller, Full correlation analysis of conformational protein dynamics, *Proteins* **70**, 1294 (2008).
- ⁵⁰S. Brandt, F. Sittel, M. Ernst, and G. Stock, Machine learning of biomolecular reaction coordinates, *J. Phys. Chem. Lett.* **9**, 2144 (2018).
- ⁵¹F. Sittel and G. Stock, Perspective: Identification of collective coordinates and metastable states of protein dynamics, *J. Chem. Phys.* **149**, 150901 (2018).
- ⁵²The number of ~ 30 correlated contacts obtained from MoSAIC for a resolution parameter $\gamma = 0.5$ agrees with the results obtained in Ref. 13, but differs to the results of Ref. 36 that mistakenly included hydrogen atoms in the contact definition, which resulted in ~ 85 correlated contacts.
- ⁵³B. Hess, C. Kutzner, D. van der Spoel, and E. Lindahl, Gromacs 4: Algorithms for highly efficient, load-balanced, and scalable molecular simulation, *Journal of Chemical Theory and Computation* **4**, 435 (2008).

- ⁵⁴V. Hornak, R. Abel, A. Okur, B. Strockbine, A. Roitberg, and C. Simmerling, Comparison of multiple Amber force fields and development of improved protein backbone parameters, *Proteins* **65**, 712 (2006).
- ⁵⁵R. B. Best and G. Hummer, Optimized molecular dynamics force fields applied to the helix-coil transition of polypeptides, *J. Phys. Chem. B* **113**, 9004 (2009).
- ⁵⁶K. Lindorff-Larsen, S. Piana, K. Palmo, P. Maragakis, J. L. Klepeis, R. O. Dror, and D. E. Shaw, Improved side-chain torsion potentials for the amber ff99sb protein force field., *Proteins* **78**, 1950 (2010).
- ⁵⁷W. L. Jorgensen and J. D. Madura, Temperature and size dependence for monte-carlo simulations of tip4p water, *Mol. Phys.* **56**, 1381 (1985).
- ⁵⁸F. Sittel, A. Jain, and G. Stock, Principal component analysis of molecular dynamics: On the use of Cartesian vs. internal coordinates, *J. Chem. Phys.* **141**, 014111 (2014).
- ⁵⁹H. Sanabria et al., Resolving dynamics and function of transient states in single enzyme molecules, *Nat. Commun* **11**, 1231 (2020).
- ⁶⁰D. Hardoon, S. Szedmak, and Shawe-Taylor, Canonical correlation analysis: an overview with application to learning methods, *Neural Comput.* **16**, 2639 (2004).
- ⁶¹F. Briki and D. Genest, Canonical analysis of correlated atomic motions in dna from molecular dynamics simulation, *Biophys. Chem.* **52**, 35 (1994).
- ⁶²X.-Q. Yao and D. Hamelberg, Detecting functional dynamics in proteins with comparative perturbed-ensembles analysis, *Acc. Chem. Res.* **52**, 3455 (2019).
- ⁶³X.-Q. Yao and D. Hamelberg, Residue–residue contact changes during functional processes define allosteric communication pathways, *J. Chem. Theory Comput.* **18**, 1173 (2022).
- ⁶⁴F. Pedregosa et al., Scikit-learn: Machine learning in Python, *J. Mach. Learn. Res.* **12**, 2825 (2011).

Supplementary Material for:

Accurate estimation of the normalized mutual information of multidimensional data

Daniel Nagel,¹ Georg Diez,¹ and Gerhard Stock¹

*Biomolecular Dynamics, Institute of Physics, University of Freiburg, 79104 Freiburg,
Germany^{a)}*

(Dated: 18 July 2024)

^{a)}Electronic mail: stock@physik.uni-freiburg.de

I. ALTERNATIVE INVARIANT MEASURES

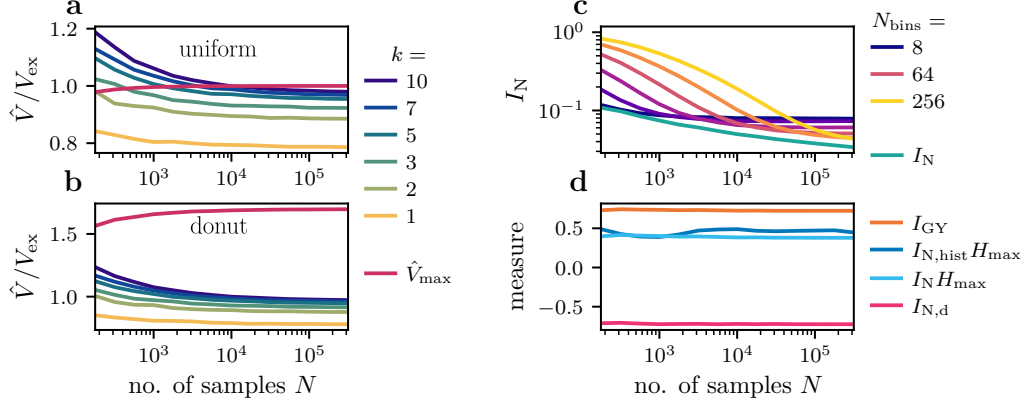


FIG. 1. Estimating the 2d volume via Eq. (1) (a+b) Estimation of the normalized volumes of various 2D distributions, using the k -nn estimator [Eq. (1), $k \in [1, 10]$] and the boundary estimate [Eq. (24), red lines]. Shown as a function of sample size N , the results are shown for (a) a uniform distribution ($x, y \in [0, 1]$) and (b) uniformly distributed data in a donut-shaped area $r = \sqrt{x^2 + y^2} \in [0.5, 1]$. (c+d) Accuracy of the new k -nn estimator of the NMI [Eq. (8)], obtained for a 2D toy model [Eq. (33)]. (c) Comparison of k -nn estimation of the NMI, shown as green line, with the discrete NMI estimation (2D binning) of the data are shown (colored lines) for various numbers of bins. (d) Convergence comparison of the MI estimator I [Eq. (20)], the I_{GY} [Eq. (17)], and the NMI estimators based on the relative entropy I_N [Eq. (31)], 2D binning $I_{N, \text{hist}}$, and the differential entropy $I_{N, d}$ [Eq. (18)]. H_{max} corresponds to the highest possible entropy, that is, the entropy of a uniform distribution, for a given number of samples N .

As mentioned in the main paper, one could also estimate the volume of by relying on the mean k -nn radius, namely

$$\hat{V}_r(X, Y) = \frac{N}{k} c_{d_X} c_{d_Y} \langle 2\varepsilon \rangle^{d_X + d_Y}, \quad (1)$$

where N is the number of data points, ε the k -th nearest neighbor distance, c_d the volume element, and d the dimensionality. In Fig. 1a,b the estimator is applied to the two examples discussed in the main paper, see Fig. 1. While all estimators converge rapidly, we find that for small k there is a systematic bias to underestimate the volume.

Following the arguments of the main paper to ensure correct factorization, we define the partial volumes by

$$\hat{V}_r(X, Y) = \hat{V}_r(X) \hat{V}_r(Y) \quad (2)$$

$$\Rightarrow \hat{V}_r(X) = \sqrt{\frac{N}{k}} c_{d_X} \langle 2\varepsilon \rangle^{d_X}. \quad (3)$$

Therewith, we get directly the invariant measures

$$\ln m_r(X) = -\ln c_{d_X} - d_X \ln \langle 2\varepsilon \rangle, \quad (4)$$

$$\ln m_r(X, Y) = -\ln(c_{d_X} c_{d_Y}) - (d_X + d_Y) \ln \langle 2\varepsilon \rangle. \quad (5)$$

To define the entropy estimators Eq. (31) and Eq. (32) this results in a rescaled k -th nearest neighbor radius of

$$\tilde{\varepsilon}_r = \frac{\varepsilon}{\langle \varepsilon \rangle}. \quad (6)$$

In Fig. 1c,d we compare the effect of the volume estimation on the NMI estimator I_N . It is clearly visible that for a distribution without fixed supports the border effects are negligible and results are in good agreement with the other volume definition, see Fig. 2 in the main paper.

II. RUNTIME COMPARISON

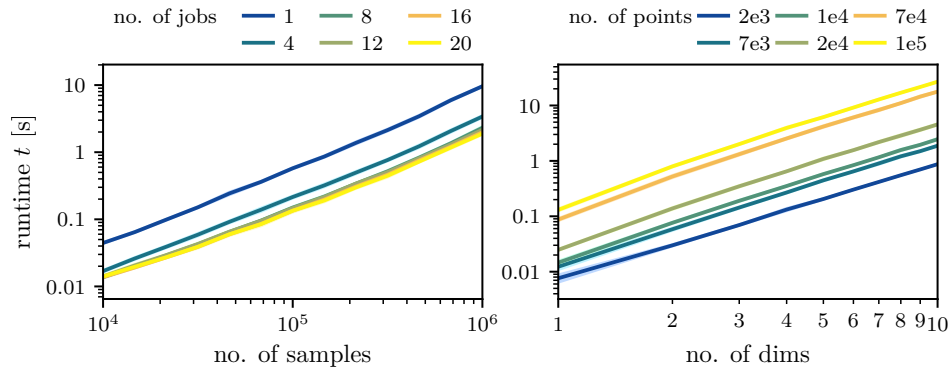


FIG. 2. Runtime comparison of the here presented NMI estimator on synthetic data \mathbf{x}, \mathbf{y} using an Intel® Core™ i9-10900 CPU. (left) Runtime depending on the no. of samples and jobs for 1D dimensional data, and (right) runtime depending on the no. of dimensions and samples. In the case of protein dynamics, this could result in a runtime of ≈ 24 h (≈ 1 h) for 1100 (230) backbone dihedral angles ($d = 1$) using $N = 10^5$ frames. In case of Cartesian coordinates ($d = 3$), this could result in a runtime of ≈ 24 h (≈ 1 h) for 900 (190) residues using $N = 10^4$ frames. Data are drawn randomly according to $x_i = \mathcal{N}(\mu = \pm 1, \sigma^2 = 1)$, where \mathcal{N} refers to a normal distribution, and the sign alternates for successive samples, and $y_i = x_i + 0.2 \mathcal{N}(\mu = 0, \sigma^2 = 1)$. For this benchmark we used $k = 3$.

III. ROTATIONAL FIT

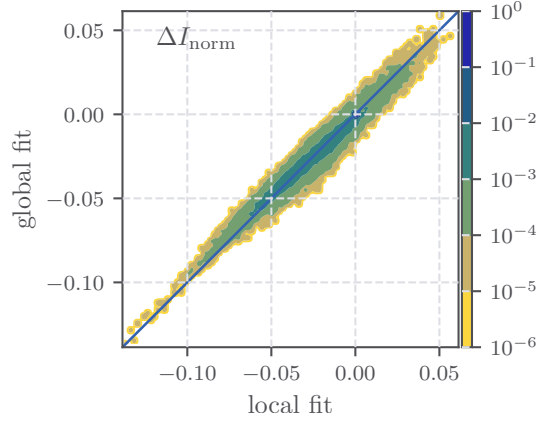


FIG. 3. Comparison of the relative differences between the local and the global fitting procedure for T4L. Shown is the joint probability distribution of the mutual information difference $\Delta I_N = I_N^{\text{closed}} - I_N^{\text{open}}$ computed using a local and global fit. In the local fitting procedure, the collective rotation and translation effects were eliminated by executing a root mean square deviation (RMSD) fit to the structure featuring the minimal average RMSD concerning all other frames within each distinct conformation (open and closed). Conversely, in the global fitting approach, the frame characterized by the minimum average RMSD relative to the complete trajectory was employed.

IV. LINEAR PEARSON CORRELATION OF T4L

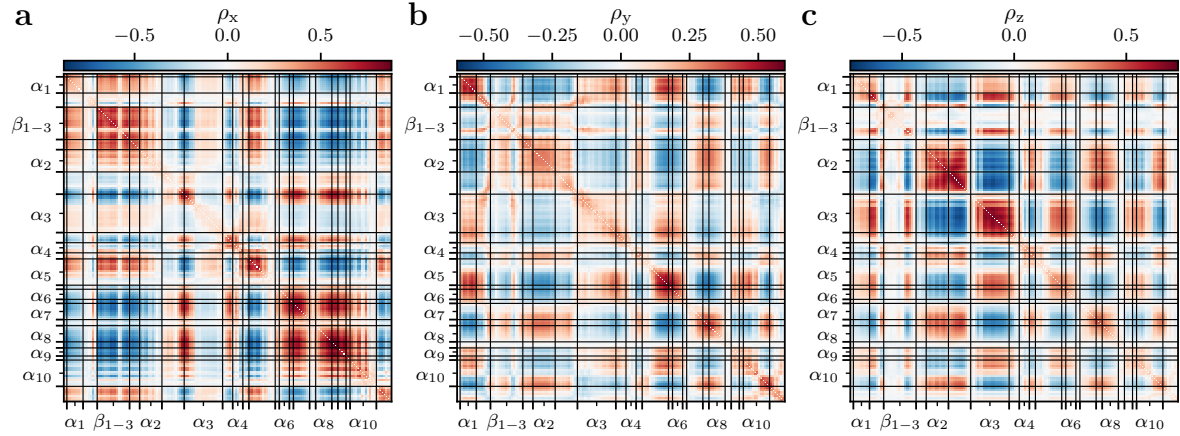


FIG. 4. The contributions of the individual directions x, y and z to the linear correlation between the Cartesian coordinates of the C_α -atoms of T4 lysozyme. Focusing on the relationship between, e.g., the α_6 and the α_8 helix, there is a large difference between the Cartesian correlation and normalized mutual information (compare Fig. 3a and c). This can be explained by the fact even though this region is correlated in all directions, the sign differs. It is positive for the x -direction and negative for the y - and z -directions which results in a cancelation of the correlation.

V. CANONICAL CARTESIAN CORRELATION

The Pearson correlation coefficient has the major drawback of not respecting correlations between different directions in the Cartesian space i and j when $i \neq j$, $i, j \in \{x, y, z\}$. Therefore, even strongly linear couplings between two sets of multidimensional variables can not be resolved (see Fig. 4). As a remedy, canonical correlation analysis tries to identify linear transformations that transform both variables in such a way that the resulting *canonical variables* feature maximum correlation. It can be shown,¹ that the canonical correlation coefficient can be calculated as

$$\rho_C = \sqrt{\frac{1}{3} \text{tr}(R)}, \quad (7)$$

where R is given by

$$R = R_{11}^{-1} R_{12} R_{22}^{-1} R_{21}, \quad (8)$$

and R_{ij} can be calculated as

$$R_{nm} = \begin{pmatrix} \langle \delta x_n \delta x_m \rangle & \langle \delta x_n \delta y_m \rangle & \langle \delta x_n \delta z_m \rangle \\ \langle \delta y_n \delta x_m \rangle & \langle \delta y_n \delta y_m \rangle & \langle \delta y_n \delta z_m \rangle \\ \langle \delta z_n \delta x_m \rangle & \langle \delta z_n \delta y_m \rangle & \langle \delta z_n \delta z_m \rangle \end{pmatrix}. \quad (9)$$

Here, $n, m \in \{1, 2\}$ denote the sets of variables 1 and 2, that is, the Cartesian coordinates of two C_α -atoms and $\delta\alpha$ are standard normalized variables $\delta\alpha = \alpha - \langle\alpha\rangle / \sqrt{\langle(\alpha - \langle\alpha\rangle)^2}$, where α can denote x, y and z . The resulting canonical correlation matrix for T4L is shown in Fig. 5 on the right-hand side. For comparison, the sum of the absolute contributions in x, y and z (shown in Fig. 4) directions is shown in Fig. 5 on the left-hand side.

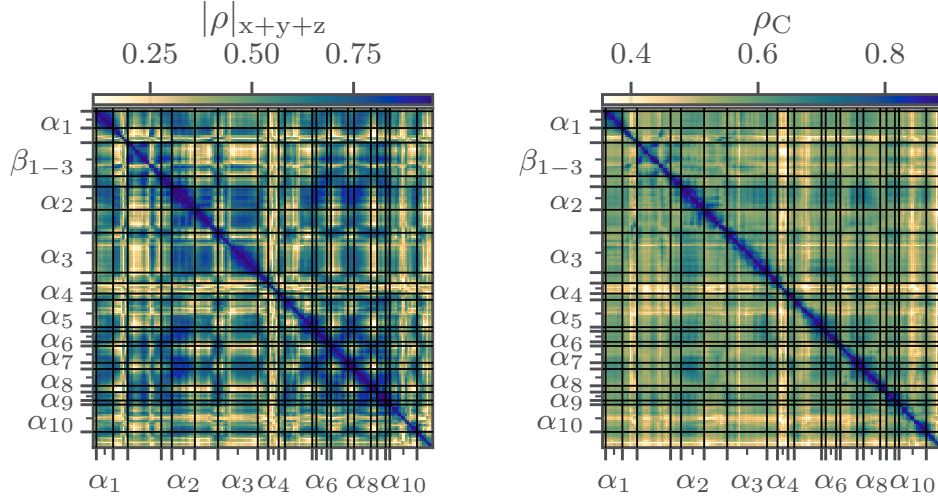


FIG. 5. Comparing linear Cartesian correlation measures for T4L. On the left-hand side, the absolute correlation contributions of each direction (see Fig. 4) are summed up, while on the right-hand side the canonical correlation is shown.

VI. FLEXIBILITY: ROOT-MEAN-SQUARE-FLUCTUATIONS

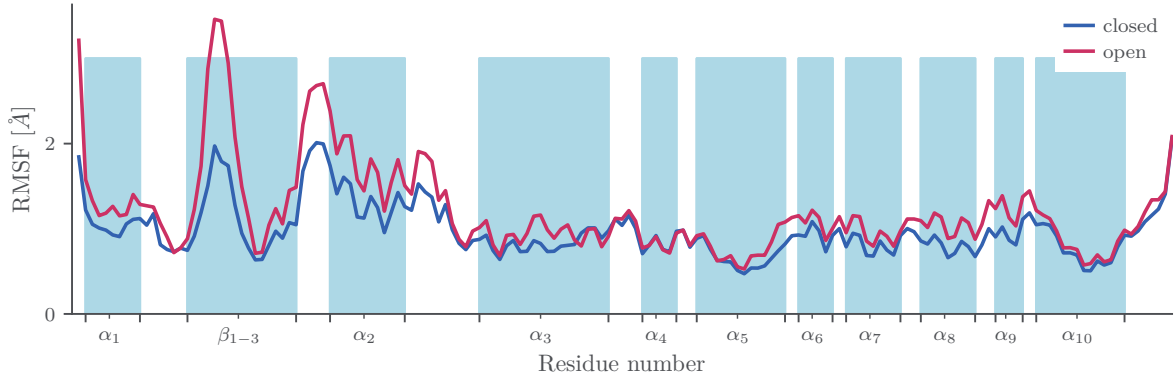


FIG. 6. The root-mean-square-fluctuation (RMSF) $\sqrt{\langle(\mathbf{x}_i - \langle\mathbf{x}_i\rangle)^2\rangle}$ as a function for every C_α -atom in the system. The RMSF was calculated for both the closed and open conformation. While the lower part of T4L ($\alpha_1 - \alpha_2$) shows a larger difference in RMSF in both conformations, the upper part seems more rigid. This is especially the case for the α_4 and α_{10} helices.

REFERENCES

- ¹F. Briki and D. Genest, Canonical analysis of correlated atomic motions in dna from molecular dynamics simulation, *Biophys. Chem.* **52**, 35 (1994).
- ²G. Diez, D. Nagel, and G. Stock, Correlation-based feature selection to identify functional dynamics in proteins, *J. Chem. Theory Comput.* **18**, 5079 – 5088 (2022).

Contacts	p_{open}	p_{closed}	Δp	$\langle \rho \rangle_{C_1}$
$r_{4,60}$	0.94	0.00	0.94	0.82
$r_{4,63}$	0.92	0.00	0.92	0.81
$r_{4,13}$	0.91	0.00	0.91	0.81
$r_{4,29}$	0.96	0.00	0.96	0.78
$r_{22,137}$	0.00	0.89	0.88	0.77
$r_{4,64}$	1.00	0.06	0.93	0.76
$r_{8,67}$	0.00	0.96	0.96	0.76
$r_{22,141}$	0.00	0.83	0.83	0.76
$r_{21,141}$	0.00	0.80	0.80	0.76
$r_{2,64}$	0.52	0.00	0.52	0.76
$r_{7,71}$	0.01	0.97	0.96	0.74
$r_{4,71}$	0.00	0.92	0.92	0.72
$r_{21,142}$	0.00	0.59	0.59	0.71
$r_{7,12}$	1.00	0.17	0.82	0.70
$r_{8,64}$	0.00	0.84	0.84	0.69
$r_{4,68}$	0.00	0.84	0.84	0.66
$r_{8,13}$	0.97	0.21	0.76	0.65
$r_{3,67}$	0.98	0.13	0.85	0.64
$r_{8,12}$	1.00	0.26	0.73	0.62
$r_{11,30}$	0.26	0.92	0.66	0.57
$r_{4,72}$	0.00	0.12	0.12	0.77
$r_{20,142}$	0.00	0.08	0.08	0.77
$r_{8,68}$	0.00	0.05	0.05	0.76
$r_{1,64}$	0.05	0.00	0.05	0.72
$r_{30,145}$	0.00	0.05	0.05	0.72
$r_{5,60}$	0.15	0.00	0.15	0.71
$r_{20,145}$	0.00	0.09	0.09	0.70
$r_{5,64}$	0.04	0.00	0.04	0.64
$r_{24,105}$	0.00	0.08	0.08	0.63
$r_{29,64}$	0.00	0.12	0.12	0.60
$r_{11,20}$	0.03	0.26	0.24	0.58
$r_{2,67}$	0.03	0.00	0.03	0.58
$r_{75,88}$	0.85	0.31	0.54	0.48
$r_{11,18}$	0.17	0.85	0.68	0.46
$r_{3,75}$	0.00	0.32	0.32	0.45
$r_{10,104}$	0.00	0.35	0.35	0.42
$r_{7,100}$	0.12	0.60	0.47	0.38
$r_{29,104}$	0.58	0.98	0.40	0.38
$r_{84,103}$	0.26	0.81	0.56	0.37
$r_{31,69}$	0.44	0.07	0.37	0.34
$r_{104,145}$	0.18	0.52	0.34	0.29
$r_{14,20}$	0.36	0.02	0.34	0.21
$r_{81,108}$	0.53	0.84	0.30	0.13

TABLE I. List of 43 inter-residue contacts that mediate the open \leftrightarrow closed transition of T4L: (Top): 20 highly correlated contacts that are most important for the open-closed transition as they are highly correlated $\langle |\rho| \rangle_{C_1}$ in the MoSAIC² analysis of cluster 1 and feature a high change in contact probability $\Delta p = |p_{\text{open}} - p_{\text{closed}}|$. (Middle): 12 contacts, that are also highly correlated, but exhibit contact probability changes $\Delta p_C \leq 0.3$. (Bottom): 11 contacts that feature a high contact probability change $\Delta p_C \geq 0.3$, but are not significantly correlated to the coordinates describing the open-closed transition $\langle |\rho| \rangle_{C_1} \leq 0.5$.